

# Evidence for a maximum mass cut-off in the neutron star mass distribution and constraints on the equation of state

Justin Alsing<sup>1\*</sup>, Hector O. Silva<sup>2,3</sup>, Emanuele Berti<sup>3,4</sup>

<sup>1</sup> Center for Computational Astrophysics, Flatiron Institute, 162 5th Avenue, New York, NY 10010, USA

<sup>2</sup> eXtreme Gravity Institute, Department of Physics, Montana State University, Bozeman, MT 59717 USA

<sup>3</sup> Department of Physics and Astronomy, The University of Mississippi, University, MS 38677-1848, USA

<sup>4</sup> CENTRA, Departamento de Física, Instituto Superior Técnico, Universidade de Lisboa, Avenida Rovisco Pais 1, 1049 Lisboa, Portugal

Accepted ; Received ; in original form

## ABSTRACT

We infer the mass distribution of neutron stars in binary systems using a flexible Gaussian mixture model and use Bayesian model selection to explore evidence for multi-modality and a sharp cut-off in the mass distribution. We find overwhelming evidence for a bimodal distribution, in agreement with previous literature, and report for the first time positive evidence for a sharp cut-off at a maximum neutron star mass. We measure the maximum mass to be  $2.0M_{\odot} < m_{\max} < 2.2M_{\odot}$  (68%),  $2.0M_{\odot} < m_{\max} < 2.6M_{\odot}$  (90%), and evidence for a cut-off is robust against the choice of model for the mass distribution and to removing the most extreme (highest mass) neutron stars from the dataset. If this sharp cut-off is interpreted as the maximum stable neutron star mass allowed by the equation of state of dense matter, our measurement puts constraints on the equation of state. For a set of realistic equations of state that support  $> 2M_{\odot}$  neutron stars, our inference of  $m_{\max}$  is able to distinguish between models at odds ratios of up to 12 : 1, whilst under a flexible piecewise polytropic equation of state model our maximum mass measurement improves constraints on the pressure at  $3 - 7\times$  the nuclear saturation density by  $\sim 30 - 50\%$  compared to simply requiring  $m_{\max} > 2M_{\odot}$ . We obtain a lower bound on the maximum sound speed attained inside the neutron star of  $c_s^{\max} > 0.63c$  (99.8%), ruling out  $c_s^{\max} < c/\sqrt{3}$  at high significance. Our constraints on the maximum neutron star mass strengthen the case for neutron star-neutron star mergers as the primary source of short gamma-ray bursts.

**Key words:** stars: neutron – equation of state

## 1 INTRODUCTION

The distribution of neutron star (NS) masses encodes a wealth of information about NS physics: NS formation channels, compact binary evolution via mass accretion, and the equation of state (EoS) of matter at ultra-high densities in the NS interior all leave distinct observable signatures on the NS mass distribution. A large enough set of NS mass measurements required for detailed study of the mass distribution has only become available relatively recently (Valentim et al. 2011; Özel et al. 2012; Kiziltan et al. 2013; Antoniadis et al. 2016) thanks mainly to a sustained and ongoing effort in radio timing of pulsars in binary systems, with earlier studies being limited to challengingly small sample sizes (Joss & Rappaport 1976; Finn 1994; Thorsett & Chakrabarty 1999; Schwab et al. 2010).

Previous studies have reported strong evidence for a bimodal NS mass distribution (Valentim et al. 2011; Özel et al. 2012; Kiziltan et al. 2013; Antoniadis et al. 2016), with one peak at  $\sim 1.3M_{\odot}$  and a second peak around  $\sim 1.5 - 1.7M_{\odot}$ . This is expected physically, since different formation and evolution channels result in NS masses clustered around different values: see Horvath & Valentim (2016) and references therein for a recent review.

In addition to being multimodal, it is possible that the mass distribution has a sharp cut-off at the highest stable mass supported by the EoS of NS matter,  $m_{\max}$ . The observation of a sharp cut-off and hence the determination of  $m_{\max}$  would put important constraints on the EoS, and it is also interesting as it delineates the low-mass limit of stellar mass black holes (Fryer & Kalogera 2001). Recent measurement of NSs with masses close to  $2M_{\odot}$  (Antoniadis et al. 2013; Demorest et al. 2010; Fonseca et al. 2016) has already put significant constraints on the EoS, and the requirement

\* e-mail: jalsing@flatironinstitute.org

that  $> 2M_{\odot}$  NSs are supported has become one of the cornerstones of observational constraints on the nuclear EoS at ultra-high densities.

Whilst observations of  $2M_{\odot}$  NS puts a robust lower bound on  $m_{\max}$ , obtaining a strongly constraining upper limit has proven more elusive. From a theoretical perspective, requiring that the EoS satisfies causality and our knowledge of nuclear matter at low densities provides a loose upper limit of  $m_{\max} < 2.9M_{\odot}$ , as shown by Kalogera & Baym (1996), following an earlier calculation by Rhoades Jr & Ruffini (1974). More recently, Lawrence et al. (2015) and Fryer et al. (2015) obtained an upper bound on  $m_{\max}$  from analysis of short gamma-ray bursts (GRBs). They argued that NS mergers only produce short GRBs if the core of the remnant collapses quickly to a black hole, and this is only possible for EoSs with relatively low  $m_{\max}$ . For EoSs with too high a maximum mass, only a tiny fraction of NS-NS mergers are able to produce GRBs; therefore if GRBs are primarily produced in NS-NS mergers then this would require a merger rate much higher than canonical values, severely stretching our understanding of binary evolution. Based on this argument Fryer et al. (2015) find  $m_{\max} < 2.2 - 2.3M_{\odot}$ . Lawrence et al. (2015) similarly find  $m_{\max} < 2.2 - 2.5M_{\odot}$  ( $m_{\max} < 2.2M_{\odot}$  assuming the rotation of the remnant is limited by mass shedding, and  $m_{\max} < 2.5M_{\odot}$  in the limiting case where the remnant has no angular momentum).

In a recent study of the mass distribution of millisecond pulsars, Antoniadis et al. (2016) considered the possibility of a sharp truncation in the mass distribution and obtained a posterior distribution for  $m_{\max}$  peaked at  $\simeq 2.1M_{\odot}$  but with reasonably large uncertainties, and from their small sample size (32 millisecond pulsars) significant evidence for or against a sharp cut-off could not be firmly established.

In this work we study the distribution of NS masses using all available NS mass measurements and explore the case for a sharp cut-off in the mass distribution due to the EoS. While previous studies of the mass distribution have split the NS sample by rotation period or other characteristics that are intended to separate out different accretion histories (Valentim et al. 2011; Özel et al. 2012; Kiziltan et al. 2013; Antoniadis et al. 2016), here we take a different approach and model the mass distribution for the whole population together using a flexible Gaussian mixture model. The mixture model has the advantage that it can naturally elicit subpopulations populating distinct modes of the distribution, and is flexible enough to capture highly non-Gaussian distributions; this allows us to analyze all the NS mass data together to obtain the strongest possible constraints on  $m_{\max}$ .

The structure of this paper is as follows. In §2 we describe the NS mass measurements. In §3 we describe the truncated Gaussian mixture models used to model the mass distribution, and the Bayesian parameter inference and model selection approaches are covered in §4. The results for the inferred mass distribution are discussed in §5, and the evidence for and constraints on a cut-off in the NS mass distribution are presented in §5.1. In §6 we explore the implications of the inferred  $m_{\max}$  on the NS EoS, computing constraints on a set of realistic EoSs in §6.1 and on a parameterized piecewise-polytropic EoS in §6.2, including constraints on the maximum sound speed in NS matter. Discussion and conclusions are in §7.

## 2 NEUTRON STAR MASS MEASUREMENTS

In this section we describe the NS mass measurements that constitute the dataset used in this work, summarized in Table 1<sup>1</sup>. For systems with measurements of two or more post-Keplerian parameters (or alternatively mass ratio or companion mass) we assume Gaussian mass likelihoods taken from the references in Table 1, and similarly for x-ray/optical observations. For systems where only the total mass or mass ratio are measured, we combine these measurements with the observed mass function to form the likelihoods given in Eqs. (3)–(4) below. For a recent review of NS mass measurements see Özel & Freire (2016).

### 2.1 Pulsars with radio timing

Radio timing of pulsars in binary systems yields precise measurements of the Keplerian orbital parameters, in particular, the orbital period  $P_b$ , eccentricity  $e$  and projected semi-major axis  $x_p$  of the pulsar’s orbit. The orbital period and projected semi-major axis together determine the mass function  $f$ ,

$$f = \left(\frac{2\pi}{P_b}\right)^2 \frac{x_p^3}{G} = \frac{m_c^3 \sin^3 i}{(m_p + m_c)^2}, \quad (1)$$

where  $m_p$  and  $m_c$  are the pulsar and companion mass, and  $i$  is the orbital inclination. Whilst the mass function is sensitive to the component masses, with three degenerate unknowns additional constraints are required to determine the component masses of the system.

For sufficiently compact binaries, it’s also possible to measure post-Keplerian parameters describing relativistic effects on the orbital motion, that are also functions of the component masses and orbital inclination. In particular, the periastron precession  $\dot{\omega}$ , Einstein delay  $\gamma$ , shape and range of the Shapiro delay  $s$  and  $r$ , and the period derivative  $\dot{P}_b$  due to gravitational wave damping are all observable and sensitive to the component masses: see e.g. Stairs (2003) and references therein. Measurement of two or more post-Keplerian parameters along with the mass function breaks the degeneracies and leads to the highest precision measurements of the component masses  $m_p$  and  $m_c$ .

If the projected semi-major axis of the companion’s orbit can also be determined, either by radio timing if it is also a pulsar, or by phase-resolved optical spectroscopy if it is optically bright, one can also determine the mass ratio of the binary  $q$ ,

$$q = \frac{m_c}{m_p} = \frac{x_p}{x_c}. \quad (2)$$

In cases where the companion is a main sequence star or white dwarf, the spectrum of the companion also contains information about its composition, that in turn provides an independent constraint on the companion mass  $m_c$ . Although these companion mass measurements are stellar-model dependent, mappings between spectral properties and mass have reached a satisfactory level of sophistication for accurate (and robust) mass determination (Tremblay et al. 2013; Althaus et al. 2013; Istrate et al. 2014; Tremblay et al. 2015).

<sup>1</sup> A database of mass measurements is maintained at [HTTPS://STELLARCOLLAPSE.ORG](https://stellarcollapse.org), which was useful in compiling the data in Table 1.

Systems where the mass function and two or more additional constraints have been measured (either post-Keplerian parameters,  $q$  or  $m_c$ ) typically yield precise pulsar mass measurements with (close to) Gaussian uncertainties. For these systems we will assume Gaussian mass likelihoods  $P(\mathbf{d}|m_p)$ , taking the mean and variance reported in the relevant radio timing analysis paper as given in Table 1.

In some cases, the only additional constraint available is a measurement of the periastron precession  $\dot{\omega}$ , that effectively provides a measurement of the total binary mass  $m_T = m_p + m_c$ . In these cases the pulsar mass can still be constrained, but the likelihood for  $m_p$  resulting from the under-constrained measurements is highly non-Gaussian, and this must be properly accounted for. We construct the pulsar-mass likelihood from the measured total mass  $\hat{m}_T$  and mass function  $\hat{f}$  as follows:

$$\begin{aligned}
 P(\mathbf{d}|m_p) &\propto \iint P(\hat{m}_T, \hat{f}|m_p, m_T, i) P(m_T) P(i) di dm_T \\
 &\propto \iint P(\hat{m}_T|m_T) P(\hat{f}|f(m_p, m_T, i)) \\
 &\quad \times P(m_T) P(i) di dm_T \\
 &\propto \iint \exp\left[-\frac{(m_T - \hat{m}_T)^2}{2\sigma_{m_T}^2}\right] \\
 &\quad \times \delta\left(f(m_p, m_T, i) - \hat{f}\right) \sin i di dm_T \\
 &= \int \frac{\exp\left[-\frac{(m_T - \hat{m}_T)^2}{2\sigma_{m_T}^2}\right] dm_T}{\frac{3(m_T - m_p)^3}{m_T^2} \left[\frac{\hat{f} m_T^2}{(m_T - m_p)^3}\right]^{\frac{1}{3}} \left[1 - \frac{\hat{f}^{2/3} m_T^{4/3}}{(m_T - m_p)^2}\right]^{\frac{1}{2}}}, \tag{3}
 \end{aligned}$$

where in the second line we assume the mass function and total mass measurements are independent, in the third line we assume Gaussian uncertainties on  $m_T$ , negligible uncertainties on  $\hat{f}^2$  and uniform priors over  $\cos i$  and  $m_T$ , and in the final line we analytically integrate out the delta function. The resulting pulsar mass likelihood function is given by the final line above.

Similarly, there are some cases where the only measurements available are the mass function  $\hat{f}$  and the mass ratio  $\hat{q}$  from phase-resolved optical spectroscopy. These under-constrained systems also result in highly non-Gaussian pulsar mass likelihoods. In a similar vein to Eq. (3), for these systems we can derive a likelihood:

$$\begin{aligned}
 P(\mathbf{d}|m_p) &\propto \iint P(\hat{q}, \hat{f}|m_p, q, i) di dq \\
 &\propto \iint P(\hat{q}|q) P(\hat{f}|f(m_p, q, i)) P(q) P(i) di dq \\
 &\propto \iint \exp\left[-\frac{(q - \hat{q})^2}{2\sigma_q^2}\right] \delta\left(f(m_p, q, i) - \hat{f}\right) \sin i di dq \\
 &= \int \frac{\exp\left[-\frac{(q - \hat{q})^2}{2\sigma_q^2}\right] dq}{\frac{3m_p}{q(q+1)^2} \left[\frac{\hat{f}q(q+1)^2}{m_p}\right]^{\frac{1}{3}} \left[1 - \left(\frac{\hat{f}q(q+1)^2}{m_p}\right)^{\frac{2}{3}}\right]^{\frac{1}{2}}}, \tag{4}
 \end{aligned}$$

<sup>2</sup> Uncertainties on the mass function from radio timing are typically very small,  $\lesssim 0.1\%$  or less, so the delta-function approximation is well justified.

where similarly in the second line we assume the mass function and mass ratio measurements are independent, in the third line we assume Gaussian uncertainties on  $q$ , negligible uncertainties on  $\hat{f}$  and uniform priors over  $\cos i$  and  $q^3$ , and in the final line we analytically integrate out the delta function.

For systems where only  $m_T$  or  $q$  were measured in addition to the mass function we assume pulsar mass likelihoods given by Eqs. (3) and (4), respectively.

## 2.2 X-ray/optical mass measurements

It is also possible to measure masses of NSs with high and low stellar mass companions using x-ray and optical observations.

For NSs with high-mass companions, eclipsing x-ray binaries where the companion blocks the x-rays from the pulsar during part of the orbit can yield mass measurements. X-ray observations of the pulsar give the Keplerian parameters  $P_b$ ,  $e$ ,  $x_p$  and the time and longitude of periastron, as well as the duration of the eclipse. Optical observations of the companion allow determination of its velocity amplitude, projected rotational velocity and amplitude of ellipsoidal variation. With these measurements in hand, it is possible to solve for the parameters of the binary system, including the NS mass. For NSs with low-mass companions, observations of thermonuclear x-ray bursts can provide measurements of their masses and radii. Typically, mass constraints from x-ray and optical observations are less precise than radio timing constraints and may be subject to systematic biases: see Özel et al. (2012); Falanga et al. (2015); Özel & Freire (2016) and references therein. Nonetheless, since all of these measurements are unlikely to be systematically biased in the same direction and make up a minority fraction of the dataset, we include them in our analysis (performing a sensitivity test to removing these data in §5.1). For x-ray/optically determined masses, we assume Gaussian mass likelihoods taken from the relevant literature (see Table 1).

The full NS mass dataset and associated literature is summarized in Table 1.

## 3 MODEL FOR THE NEUTRON STAR MASS DISTRIBUTION

We want a flexible parameterized model for the mass distribution that can allow for a number of key features: multiple modes coming from subpopulations with distinct formation channels and accretion histories, non-Gaussian (e.g. skewed) modes, and the possibility of a sharp truncation at some maximum mass. To this end, we model the NS mass distribution as an  $n$ -component Gaussian mixture model with a sharp cut-off at some maximum mass  $m_{\max}$ . The truncated Gaussian mixture model has all of the required features; multiple Gaussian components can capture both dis-

<sup>3</sup> A uniform prior on  $q$  might not be the most appropriate choice given knowledge of the nature of the two objects, but since the measurement uncertainties on  $q$  are typically  $\lesssim 1\%$ , the Gaussian likelihood for  $q$  should be sufficiently sharply peaked to make this highly insensitive to alternative prior choices.

name	type	$f [M_{\odot}]$	$m_T [M_{\odot}]$	$q$	$m_p [M_{\odot}]$	reference
4U1700-377	x-ray/optical				1.96±0.19	Falanga et al. (2015)
Cyg X-2	x-ray/optical				1.71±0.21	Casares et al. (2010)
SMC X-1	x-ray/optical				1.21±0.12	Falanga et al. (2015)
Cen X-3	x-ray/optical				1.57±0.16	Falanga et al. (2015)
XTE J2123-058	x-ray/optical				1.53±0.42	Gelino et al. (2002)
4U 1822-371	x-ray/optical				1.96±0.36	Munoz-Darias et al. (2005)
OA0 1657-415	x-ray/optical				1.74±0.3	Falanga et al. (2015)
J013236.7+303228	x-ray/optical				2.0±0.4	Bhalerao et al. (2012)
Vela X-1	x-ray/optical				2.12±0.16	Falanga et al. (2015)
4U1538-522	x-ray/optical				1.02±0.17	Falanga et al. (2015)
LMC X-4	x-ray/optical				1.57±0.11	Falanga et al. (2015)
Her X-1	x-ray/optical				1.073±0.36	Rawls et al. (2011)
2S 0921-630	x-ray/optical				1.44±0.1	Steeeghs & Jonker (2007)
EXO 1722-363	x-ray/optical				1.91±0.45	Falanga et al. (2015)
SAX J1802.7-2017	x-ray/optical				1.57±0.25	Falanga et al. (2015)
XTE J1855-026	x-ray/optical				1.41±0.24	Falanga et al. (2015)
B1957+20	x-ray/optical	$5 \times 10^{-6}$		69.2±0.8		Van Kerkwijk et al. (2011)
J1311-3430	x-ray/optical	$3 \times 10^{-7}$		175±3		Romani et al. (2012)
J1740-5350	x-ray/optical	0.002644		5.85±0.13		Ferraro et al. (2003)
J1816+4510	x-ray/optical	0.0017607		9.54±0.21		Kaplan et al. (2013)
J1723-2837	x-ray/optical	0.005221		3.45±0.02		van Staden & Antoniadis (2016)
J0453+1559	NS-NS				1.559±0.004	Martinez et al. (2015)
J0453+1559 comp.	NS-NS				1.174±0.004	Martinez et al. (2015)
J1906+0746	NS-NS				1.291 ±0.011	van Leeuwen et al. (2015)
J1906+0746 comp.	NS-NS				1.322±0.011	van Leeuwen et al. (2015)
B1534+12	NS-NS				1.3332±0.0010	Fonseca et al. (2014)
B1534+12 comp.	NS-NS				1.3452±0.0010	Fonseca et al. (2014)
B1913+16	NS-NS				1.4398±0.0002	Weisberg et al. (2010)
B1913+16 comp.	NS-NS				1.3886±0.0002	Weisberg et al. (2010)
B2127+11C	NS-NS				1.358±0.010	Jacoby et al. (2006)
B2127+11C comp.	NS-NS				1.354±0.010	Jacoby et al. (2006)
J0737-3039A	NS-NS				1.3381±0.0007	Kramer et al. (2006)
J0737-3039B	NS-NS				1.2489±0.0007	Kramer et al. (2006)
J1756-2251	NS-NS				1.312±0.017	Ferdman et al. (2014)
J1756-2251 comp.	NS-NS				1.258±0.017	Ferdman et al. (2014)
J1807-2500B	NS-NS				1.3655±0.0021	Lynch et al. (2012)
J1807-2500B comp.	NS-NS				1.2064±0.0020	Lynch et al. (2012)
J1913+1102	NS-NS	0.136344	2.875±0.014			Lazarus et al. (2016)
J2045+3633	NS-WD				1.33±0.3	Berezina et al. (2017)
J2053+4650	NS-WD				1.40±0.21	Berezina et al. (2017)
J1713+0747	NS-WD				1.35±0.07	Arzoumanian et al. (2017)
B1855+09	NS-WD				1.37±0.13	Arzoumanian et al. (2017)
J0751+1807	NS-WD				1.72±0.07	Desvignes et al. (2016)
J1141-6545	NS-WD				1.27±0.01	Bhat et al. (2008)
J1738+0333	NS-WD				1.47±0.07	Antoniadis et al. (2012)
J1614-2230	NS-WD				1.908±0.016	Arzoumanian et al. (2017)
J0348+0432	NS-WD				2.01±0.04	Antoniadis et al. (2013)
J2222-0137	NS-WD				1.76±0.06	Cognard et al. (2017)
J2234+0611	NS-WD				1.393±0.013	Stovall et al. (2016)
J1949+3106	NS-WD				1.47±0.43	Deneva et al. (2012)
J1012+5307	NS-WD				1.83±0.11	Antoniadis et al. (2016)
J0437-4715	NS-WD				1.44±0.07	Reardon et al. (2016)
J1909-3744	NS-WD				1.48±0.03	Arzoumanian et al. (2017)
J1802-2124	NS-WD				1.24±0.11	Ferdman et al. (2010)
J1911-5958A	NS-WD				1.34±0.08	Bassa et al. (2006)
J2043+1711	NS-WD				1.38±0.13	Arzoumanian et al. (2017)
J0337+1715	NS-WD				1.4378±0.0013	Ransom et al. (2014)
J1946+3417	NS-WD				1.828±0.022	Barr et al. (2016)
J1918-0642	NS-WD				1.29±0.1	Arzoumanian et al. (2017)
J1600-3053	NS-WD				2.3±0.7	Arzoumanian et al. (2017)
J0024-7204H	NS-WD	0.001927	1.665±0.007			Freire et al. (2017)
J0514-4002A	NS-WD	0.14549547	2.453±0.014			Freire et al. (2007)
J0621+1002	NS-WD	0.027026849	2.32±0.08			Splaver et al. (2002)
B1516+02B	NS-WD	0.000646723	2.29±0.17			Freire et al. (2008b)
J1748-2021B	NS-WD	0.0002266235	2.92±0.20			Freire et al. (2008a)
J1748-2446I	NS-WD	0.003658	2.17±0.02			Ransom et al. (2005)
J1748-2446J	NS-WD	0.013066	2.20±0.04			Ransom et al. (2005)
B1802-07	NS-WD	0.00945034	1.62±0.07			Thorsett & Chakrabarty (1999)
J1824-2452C	NS-WD	0.006553	1.616±0.007			Freire et al. (2008a)
B2303+46	NS-WD	0.246261924525	2.64±0.05			Thorsett & Chakrabarty (1999)
J1750-37A	NS-WD	0.0518649	1.97±0.15			Freire et al. (2008a)
J0045-7319	NS-MS				1.58±0.34	Nice (2003)
J1023+0038	NS-MS				1.71±0.16	Deller et al. (2012)
J1903+0327	NS-MS				1.666±0.01	Arzoumanian et al. (2017)

**Table 1.** NS mass measurements (74 in total). For systems with two or more post-Keplerian parameters measured, and x-ray/optical mass measurements, we take measured pulsar masses at face value with Gaussian uncertainties. For systems where only the mass function and total mass or mass ratio are measured, we use these data to construct the mass likelihoods given in Eqs. (3) and (4).

tinct peaks and skewed individual modes, and the possibility of a sharp cut-off can be included as a free parameter.

We consider the model space covered by varying the number of Gaussian components  $n$ , with two scenarios regarding the cut-off: either a sharp cut-off fixed at  $m_{\max} = 2.9M_{\odot}$ , or keeping  $m_{\max} < 2.9M_{\odot}$  as an additional free parameter. Exploring this model space allows us to compare models of varying complexity using Bayesian model comparison and explicitly assess the evidence for multiple modes and skewness, and to quantify evidence for a sharp cut-off at  $m_{\max} < 2.9M_{\odot}$ .

The  $n$ -component mixture model for the mass distribution is given by

$$P(m_p|\boldsymbol{\theta}) = \sum_{i=1}^n r_i \mathcal{N}(m_p|\mu_i, \sigma_i) \Theta(m_p - m_{\max}) / \Phi_i \quad (5)$$

for the pulsar mass  $m_p$ , where  $\mu_i$ ,  $\sigma_i$  and  $r_i$  denote the mean, standard deviation and relative weight of the  $i$ -th Gaussian component,  $\mathcal{N}$  denotes the Gaussian density and  $\Theta$  denotes the Heaviside function. The normalization constants  $\Phi_i \equiv \Phi(\mu_i, \sigma_i; m_{\min}, m_{\max})$  are integrals over the Gaussian components (over the allowed NS mass range):

$$\Phi(\mu, \sigma; m_{\min}, m_{\max}) = \int_{m_{\min}}^{m_{\max}} \mathcal{N}(x|\mu, \sigma) dx. \quad (6)$$

To keep the distribution normalized to unity, the weights are constrained to sum to one,  $\sum_{i=1}^n r_i = 1$ . The full set of model parameters is hence:

$$\boldsymbol{\theta} = \{\mu_1, \mu_2, \dots, \mu_n, \sigma_1, \sigma_2, \dots, \sigma_n, r_1, r_2, \dots, r_n, m_{\max}\} \quad (7)$$

We consider two cases: one with  $m_{\max}$  fixed at  $m_{\max} = 2.9M_{\odot}$ , and one with  $m_{\max} < 2.9M_{\odot}$  kept as a free model parameter. The following uniform priors are assumed for the model parameters:  $\mu_i \in [0.9, 2.9]$ ,  $\sigma_i \in [0.01, 2]$ ,  $m_{\max} \in [1.9, 2.9]$ , and a flat Dirichlet prior over the weights  $\{r_i\}$ <sup>4</sup>. We impose the additional constraint that the component means are ordered ( $\mu_1 < \mu_2 < \dots < \mu_n$ ) so that the Gaussian components are distinguishable. We assume a minimum NS mass of  $m_{\min} = 0.9M_{\odot}$  throughout. The limits of the uniform priors over  $\{\mu_i, \sigma_i, m_{\max}\}$  are carefully chosen to be broad enough to not truncate the resulting posteriors (over the range of allowed parameter values). However, choice of uniform priors is still somewhat subjective.

## 4 BAYESIAN INFERENCE OF THE NEUTRON STAR MASS DISTRIBUTION

### 4.1 Parameter inference

The goal is to infer the model parameters of the NS mass distribution from the measured masses in a Bayesian framework. The joint posterior for the masses  $m_p$  and mass-distribution model parameters  $\boldsymbol{\theta}$  given the data (for all NSs

<sup>4</sup> The flat Dirichlet prior  $\mathbf{r} \sim \text{Dir}(n; 1)$  is a uniform prior over the  $(n-1)$ -simplex defined by  $0 < r_i < 1 \forall i$  and  $\sum_{i=1}^n r_i = 1$ , ensuring that the mixture distribution Eq. (5) is proper and normalized to unity.

$\mathbf{d} = \{\mathbf{d}^i\}$ ) is given by Bayes' theorem:

$$P(\boldsymbol{\theta}, \{m_p^i\} | \mathbf{d} = \{\mathbf{d}^i\}) \propto P(\boldsymbol{\theta}) P(\mathbf{d} | \boldsymbol{\theta}, \{m_p^i\}) \propto P(\boldsymbol{\theta}) \prod_{i=1}^N P(\mathbf{d}^i | m_p^i) P(m_p^i | \boldsymbol{\theta}), \quad (8)$$

where in the second line we have exploited the conditional independence of the data on the parameters  $\boldsymbol{\theta}$  once the masses  $\{m_p^i\}$  are specified, and the assumed independence of the mass data for each NS. The posterior for  $\boldsymbol{\theta}$  marginalized over the individual masses is hence given by

$$P(\boldsymbol{\theta} | \mathbf{d}) \propto P(\boldsymbol{\theta}) \prod_{i=1}^N \int P(\mathbf{d}^i | m_p^i) P(m_p^i | \boldsymbol{\theta}) dm_p^i. \quad (9)$$

Since the mass-distribution model considered here is a truncated Gaussian mixture, the integrals on the right hand side of Eq. (9) have simple closed-form solutions for Gaussian mass-likelihoods, and are otherwise cheap to compute numerically for the remaining non-Gaussian likelihoods, i.e. Eqs. (3) and (4). We explicitly marginalize over all of the individual masses either analytically or numerically, and reconstruct the posterior  $P(\boldsymbol{\theta} | \mathbf{d})$  by sampling from Eq. (9) using nested sampling with MULTINEST (Feroz & Hobson 2008; Feroz et al. 2009; Buchner et al. 2014). Nested sampling has the advantage that it generates samples from the posterior distribution and simultaneously computes the Bayesian evidence integrals needed for performing Bayesian model selection (as required in §4.2, see below).

### 4.2 Bayesian model selection

In addition to inferring the model parameters of the mass-distribution models considered, we also want to be able to compare their relative merit and determine which model is preferred by the data. Bayesian model selection – computing the odds ratio between two models – provides a principled framework for model comparison that naturally takes into account Occam's razor, i.e., penalizing more complicated models where both models fit the data.

The odds ratio between two models  $\mathcal{M}_A$  and  $\mathcal{M}_B$  is given by

$$\mathcal{O}_{AB} = \frac{P(\mathcal{M}_A | \mathbf{d})}{P(\mathcal{M}_B | \mathbf{d})} = \frac{P(\mathbf{d} | \mathcal{M}_A) P(\mathcal{M}_A)}{P(\mathbf{d} | \mathcal{M}_B) P(\mathcal{M}_B)}, \quad (10)$$

where  $\mathcal{Z} = P(\mathbf{d} | \mathcal{M})$  is the Bayesian evidence (or marginal likelihood) for a given model  $\mathcal{M}$  given data  $\mathbf{d}$ , and the prior odds ratio  $P(\mathcal{M}_A) / P(\mathcal{M}_B)$  defines our prior relative belief in model  $A$  over model  $B$ . If we are *a priori* agnostic about the two models, the prior odds is unity and the odds ratio reduces to the Bayes factor:

$$\mathcal{K}_{AB} = \frac{P(\mathbf{d} | \mathcal{M}_A)}{P(\mathbf{d} | \mathcal{M}_B)}, \quad (11)$$

where  $\mathcal{K}_{AB} > 1$  indicates that model  $A$  is preferred by the data over model  $B$ , and vice versa for  $\mathcal{K}_{AB} < 1$ . In this study we follow the scheme of Kass & Raftery (1995) for interpreting the Bayes factor:  $2\ln\mathcal{K}_{AB} < 0$  implies no support for  $A$  over  $B$ ,  $0 < 2\ln\mathcal{K}_{AB} < 2$  support for  $A$  “worth not more than a bare mention”,  $2 < 2\ln\mathcal{K}_{AB} < 6$  positive support for  $A$ ,  $6 < 2\ln\mathcal{K}_{AB} < 10$  strong support, and  $2\ln\mathcal{K}_{AB} > 10$  very strong support.

We compute the Bayesian evidences  $\mathcal{Z}$  for the models

considered using MULTINEST nested sampling (Feroz & Hobson 2008; Feroz et al. 2009; Buchner et al. 2014).

## 5 RESULTS: THE INFERRED NEUTRON STAR MASS DISTRIBUTION

The Bayesian evidences for the space of (truncated) Gaussian mixture models are given in Table 2. The models with two and three components are preferred by the data compared to the models with one and four Gaussian components. The single-component Gaussian is strongly disfavored (with Bayes factors of  $2\ln\mathcal{K} \gtrsim 10$ ) when compared against the two and three component models, indicating very strong evidence against  $n = 1$ . The four-component model is also disfavored although less strongly, with Bayes factors of  $2\ln\mathcal{K} \gtrsim 2$  compared to the two and three component models. Comparing the two and three component models, the two component model is modestly preferred in all cases, but the difference in their Bayesian evidences is not large enough to make a strong preference for either model.

In all cases  $n = 1, \dots, 4$ , the model with the maximum NS mass as an additional free parameter is preferred. In all cases  $n \geq 2$ , the models with free  $m_{\max}$  are preferred over those with fixed  $m_{\max}$  with Bayes factors  $2\ln\mathcal{K} > 3$ : there is positive support for a sharp cut-off in the NS mass distribution at  $m_{\max} < 2.9M_{\odot}$ . This is the first major result of this paper.

Fig. 1 shows the maximum *a posteriori* (MAP) mass distributions for the four models that are most preferred by the data; the  $n = 2, 3, 4$  models with a sharp cut-off at  $m_{\max} < 2.9M_{\odot}$ , and the  $n = 2$  model with the cut-off fixed out at  $m_{\max} = 2.9M_{\odot}$  for comparison. The introduction of additional Gaussian components above  $n = 2$  modifies the shape of the second peak, but does not introduce an additional independent mode, even though this would be perfectly allowed under the model. The convergence of all models with  $n \geq 2$  to a bimodal distribution provides overwhelming support for a bimodal NS mass distribution, with no evidence for an additional distinct peak in the distribution or separation of the lower mass peak into two narrow components, as suggested in Schwab et al. (2010). This is consistent with recent literature (Valentim et al. 2011; Özel et al. 2012; Kiziltan et al. 2013; Antoniadis et al. 2016).

Fig. 2 shows the MAP mass distribution for the  $n = 2$  model with free  $m_{\max}$  with 1000 independent posterior samples plotted over the top to give a visual impression of the uncertainties on the shape of the distribution. As the most preferred model, we take this as our fiducial model moving forward.

The MAP values and 68% credible regions for the preferred  $n = 2$  component models are given in Table 3.

### 5.1 Constraints on $m_{\max}$ from the neutron star mass distribution

As discussed above, we find evidence for a sharp cut-off in the NS mass distribution under all models considered, with Bayes factors of  $2\ln\mathcal{K} > 3$  for all models  $n \geq 2$  (Table 2). The marginal posterior distribution for the maximum NS mass under the fiducial  $n = 2$  model is shown in Fig. 3. The inferred posterior is peaked at  $m_{\max} = 2.12M_{\odot}$ , with

model:	$m_{\max} = 2.9M_{\odot}$	$m_{\max} < 2.9M_{\odot}$
$n = 1$ components	-35.0	-34.8
$n = 2$ components	<b>-25.8</b>	<b>-22.7</b>
$n = 3$ components	-27.3	<b>-23.9</b>
$n = 4$ components	-30.4	<b>-25.9</b>

**Table 2.** Log Bayesian evidences  $2\ln(\mathcal{Z})$  for the set truncated Gaussian mixture models considered for the NS mass distribution, covering  $n = 1 \dots 4$  Gaussian components, each with either fixed  $m_{\max} = 2.9M_{\odot}$  or keeping  $m_{\max} < 2.9M_{\odot}$  as an additional free parameter. The four preferred models are highlighted in boldface. We perform model selection by comparing  $2\ln\mathcal{K}_{AB} = 2\ln\mathcal{Z}_A - 2\ln\mathcal{Z}_B$  to the scale of Kass & Raftery (1995) (see §4.2).

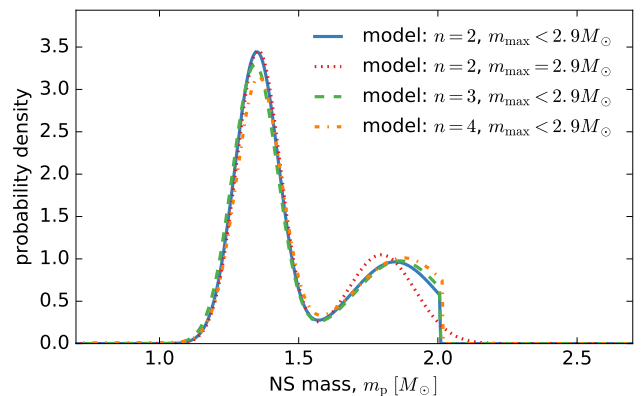


**Figure 1.** Comparison of maximum a posteriori (MAP) NS mass distributions under different model assumptions:  $n = 2$  Gaussian components with  $m_{\max} < 2.9M_{\odot}$  (preferred model; blue-solid),  $n = 2$  Gaussian components with  $m_{\max} = 2.9M_{\odot}$  (red-dashed),  $n = 3$  Gaussian components with  $m_{\max} < 2.9M_{\odot}$  (green-dashed),  $n = 4$  Gaussian components with  $m_{\max} < 2.9M_{\odot}$  (orange-dashed).

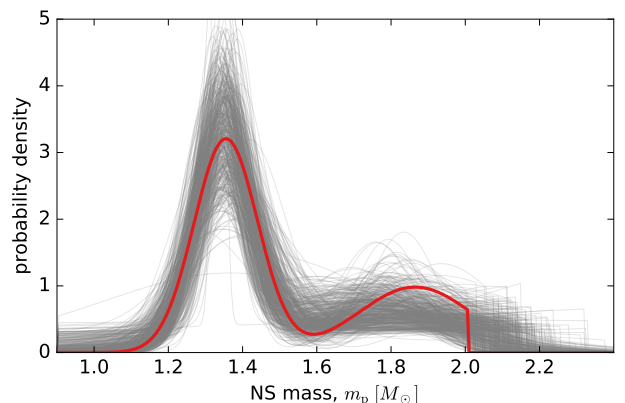


**Figure 2.** Maximum a posteriori (MAP) NS mass distribution (red) with 1000 independent posterior samples to give a visual guide for the uncertainties, under the considered model that is most preferred by the data; the  $n = 2$  component Gaussian mixture with a sharp cut-off  $m_{\max} < 2.9M_{\odot}$ .

model	$\mu_1$	$\mu_2$	$\sigma_1$	$\sigma_2$	$r_1$	$m_{\max}$
$n = 2$ components, $m_{\max} < 2.9M_{\odot}$	$1.34^{+0.03}_{-0.02}$	$1.80^{+0.15}_{-0.18}$	$0.07^{+0.02}_{-0.02}$	$0.21^{+0.18}_{-0.14}$	$0.65^{+0.08}_{-0.15}$	$2.12^{+0.09}_{-0.12}$
$n = 2$ components, $m_{\max} = 2.9M_{\odot}$	$1.34^{+0.02}_{-0.02}$	$1.78^{+0.07}_{-0.09}$	$0.07^{+0.03}_{-0.03}$	$0.12^{+0.09}_{-0.03}$	$0.66^{+0.09}_{-0.09}$	-

**Table 3.** Maximum a posteriori (MAP) values and 68% credible intervals of the 1-d marginal posteriors for the preferred  $n = 2$  component Gaussian mixture model with free  $m_{\max} < 2.9M_{\odot}$  and with  $m_{\max}$  fixed at  $2.9M_{\odot}$ . All dimensional quantities are in units of solar masses.

credible regions  $2.0M_{\odot} < m_{\max} < 2.2M_{\odot}$  (68%) and  $2.0 < m_{\max} < 2.6M_{\odot}$  (90%)<sup>5</sup>. The lower limit on the maximum mass is hard, whilst the posterior has a fat (almost flat) tail out to  $2.9M_{\odot}$ ; although the maximum mass has clearly been constrained, there persists a small but non-negligible possibility that  $m_{\max}$  is still large.

Some constraints on  $m_{\max}$  were reported in [Antoniadis et al. \(2016\)](#) who studied the distribution of millisecond pulsar masses using a similar (two component) Gaussian mixture model as used in this work. Our constraints are in good agreement with their results: cf. Fig. 10 of [Antoniadis et al. \(2016\)](#). By considering all available NS mass data we are able to provide tighter constraints and, for the first time, substantial evidence that a sharp cut-off is preferred by the data; the mass cut-off is preferred with a Bayes factor of  $2\ln\mathcal{K} > 3$ , whilst from the smaller subset of mass data considered in [Antoniadis et al. \(2016\)](#) the cut-off is only preferred with  $2\ln\mathcal{K} = 1.5$  (owing to the smaller sample). Nonetheless our results are entirely consistent with [Antoniadis et al. \(2016\)](#).

Our constraints on the maximum NS mass are also in good agreement with, and independent of, recent studies of short GRBs, where [Lawrence et al. \(2015\)](#) and [Fryer et al. \(2015\)](#) argue that  $m_{\max} \lesssim 2.2 - 2.5M_{\odot}$  is required assuming that the main source of short GRBs are NS-NS mergers. On the flip side, our constraints on the maximum NS mass show a strong preference for equations of state that produce short GRBs in NS-NS mergers. Combined with canonical values for binary NS merger rates ([Abadie et al. 2010](#); [Dominik et al. 2015](#); [Chruslinska et al. 2017](#)), our result strengthens the case for NS mergers as the primary source of short GRBs. Our results are also in good agreement with independent constraints on  $m_{\max}$  from observations of the binary neutron-star merger GW170817 ([Abbott et al. 2017](#)), which give have been used to derive upper limits  $m_{\max} < 2.17M_{\odot}$  (90%) ([Margalit & Metzger 2017](#)),  $m_{\max} < 2.33M_{\odot}$  (90%) ([Rezzolla et al. 2018](#)) and  $m_{\max} < 2.16 - 2.28M_{\odot}$  ([Ruiz et al. 2018](#)).

In the following section we discuss the sensitivity of the inferred posterior on  $m_{\max}$  to the choice of model and to key data cuts.

#### Sensitivity to data cuts

In Fig. 4 (left) we look at the impact of removing certain key NSs from the data.

We should expect that the lower limit on  $m_{\max}$

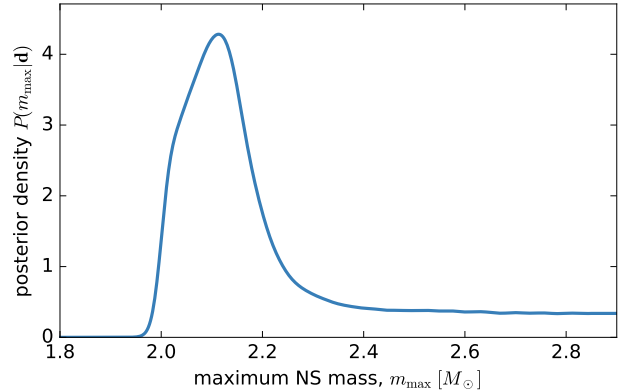


**Figure 3.** Marginal posterior distribution for  $m_{\max}$  derived from inferring the distribution of NS masses, assuming the mass-distribution can be modeled as the sum of two Gaussians with a hard cut at  $m_{\max}$ .

comes predominantly from the most massive precisely measured NSs available to date, namely J0348+0432 ( $m_p = 2.01(4)M_{\odot}$ ; [Antoniadis et al. \(2013\)](#)) and J1614-2230 ( $m_p = 1.93(2)$ ; [Demorest et al. \(2010\)](#); [Fonseca et al. \(2016\)](#)). From Fig. 4 (left; red and blue) it is evident that removing J0348+0432 or both J0348+0432 and J1614-2230 from the dataset impacts the lower limit for  $m_{\max}$ , as expected, whilst otherwise preserving the qualitative shape of the posterior. Importantly, evidence for a cut-off in the mass distribution remains even with these important systems removed, albeit at a weaker level with  $2\ln\mathcal{K} = 1.2$ .

The other high-mass NS that one might suspect has a disproportionate impact on the inferred  $m_{\max}$  is J1748-2021B<sup>6</sup> ([Freire et al. 2008a](#)). This system has a measured mass of  $m_p = 2.74(21)M_{\odot}$ , as inferred from the total mass of that binary system (c.f. Eq. (3)). Although the uncertainty on its mass is substantial, since this system has almost all of its mass-likelihood at  $m_p > 2M_{\odot}$  (with very low probability of being  $< 2M_{\odot}$ ) and such a high peak value, this system could be strongly informative on the lower limit on  $m_{\max}$  and responsible for the flat tail of the posterior density out to high values. From Fig. 4 (left; green) it is clear that removing this system has very little impact on the inference of  $m_{\max}$ .

The subset of the NS mass data that may be suspected to be contaminated by systematic errors, and hence biasing the inferred  $m_{\max}$ , are those mass measurements obtained

<sup>5</sup> Due to the fat tail of the posterior on  $m_{\max}$ , for the Bayesian credible regions we quote an iso-probability interval for the 68% credible region, and a one-tail upper limit (with a hard lower limit) for the 90% credible region.

<sup>6</sup> Other likely high-mass pulsars, such as the so-called black-widow pulsar B1957+20, are typically less extreme in their mass-likelihoods than J1748-2021B so should have an even smaller impact on the inferred  $m_{\max}$ .

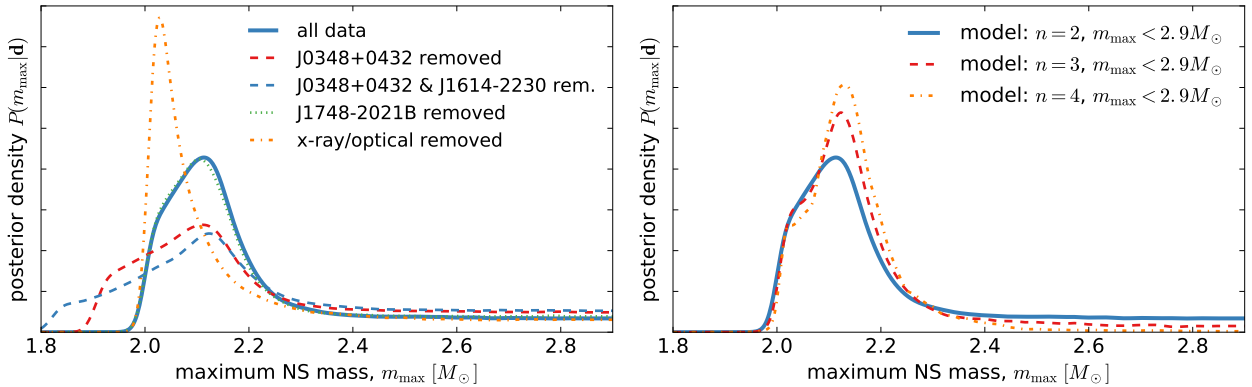


**Figure 4.** Left: Sensitivity of the inferred marginal posterior distribution for  $m_{\max}$  to removing key NSs from the dataset; keeping all NS mass data (blue-solid), removing J0348+0432 ( $m_p = 2.01(4)M_{\odot}$ ; red-dashed), removing J0348+0432 and also J1614-2230 ( $m_p = 1.93(2)$ ; blue-dashed), removing J1748-2021B ( $m_p = 2.74(21)M_{\odot}$ ; green-dashed) and removing the 21 x-ray/optical mass measurements (orange-dashed). Right: Sensitivity of the inferred marginal posterior distribution for  $m_{\max}$  to the number of Gaussian components  $n$  in the model:  $n = 2$  (fiducial; blue-solid),  $n = 3$  (red-dashed),  $n = 4$  (orange-dashed).

through optical and x-ray observations (Özel et al. 2012; Falanga et al. 2015). From Fig. 4 (left; orange) it is clear that removing the x-ray/optical mass data has a much more substantial impact on the  $m_{\max}$  posterior. This is hardly surprising, since the 21 x-ray/optical masses removed represent a substantial fraction of the total sample of 74, and they populate the higher-mass end of the distribution. Removing the x-ray/optical data shifts the posterior on  $m_{\max}$  by around  $0.1M_{\odot}$  and sharpens it (reducing the width at half-maximum by roughly a factor of two). The small shift and smearing of the posterior to higher  $m_{\max}$  when including the x-ray/optical data makes good sense, since those systems occupy the higher mass end of the distribution and may hence encourage a slightly higher cut-off. Whilst it is possible that systematic biases in the x-ray/optical mass measurements bias the  $m_{\max}$  inference, they would have to all be preferentially biased in the same direction for this effect to be significant, and even if this were the case we should expect the bias to be much smaller than the  $0.1M_{\odot}$  shift induced by removing those data completely. Crucially, positive evidence for a sharp cut-off persists with the x-ray/optical masses removed – the model with free  $m_{\max} < 2.9M_{\odot}$  is preferred over  $m_{\max} = 2.9M_{\odot}$  with a Bayes factor of  $2\ln\mathcal{K} = 2.2$  (positive support for the cut-off). The fact that removing the x-ray/optical mass measurements does not significantly change our conclusions and any bias introduced by their systematics is expected to be small adds robustness to our results.

From these sensitivity tests, we conclude that the evidence for and inference of  $m_{\max}$  is driven by the shape of the NS mass-distribution, informed by the whole population, rather than set exclusively by the most extreme objects observed (although the highest precisely measured masses dominate the lower limit on  $m_{\max}$ ). Our key conclusion – that there is evidence for a sharp cut-off in the NS mass distribution – is robust to removing key subsets of the dataset.

#### *Sensitivity to the mass distribution model*

In Fig. 4 (right) we explore the sensitivity of the inference of  $m_{\max}$  on the choice of model for the mass distribution. Clearly, the three Gaussian mixture models considered with 2-, 3- and 4-components respectively yield a very similar posterior distribution for  $m_{\max}$ , with a small shift in the peak value and modestly tighter constraints on  $m_{\max}$  as the number of components is increased. Note that the latter observation is also corroborated by the Bayesian evidences for the various models given in Table 2, i.e., the evidence for a cut-off  $m_{\max} < 2.9M_{\odot}$  versus  $m_{\max} = 2.9M_{\odot}$  increases with the number of components. The fact that the  $m_{\max}$  posterior is so insensitive to the number of components in the model is also unsurprising in light of Fig. 1; all models give a similar bimodal distribution, where the key change is in the shape of the higher-mass mode but the qualitative characteristics of the distribution are very similar.

Whilst the sample size of measured NS masses is small and we restricted our analysis to the space of Gaussian mixture models, the lack of sensitivity to the model choice seen in Fig. 4 adds robustness to our results.

#### *Selection effects and accretion*

It is possible that selection effects may be influencing our inference of the mass distribution. The mass measurements used are exclusively from NSs in binaries, so our results should not be assumed to be applicable to isolated NSs. Furthermore, Shapiro delay detection (leading to the most precise mass measurements) is easier in systems with short orbital periods and higher inclinations, and spectroscopic observations are more relevant to relatively compact systems. Whilst it is possible that these selection effects may leave some imprint on the inferred mass distribution, it seems implausible that they are responsible for the inferred hard cut-off at  $m_{\max}$ .

The high-mass end of the distribution is a strong probe of both formation of higher mass NSs and accretion physics. In the absence of a hard cut-off due to the EoS, one would ex-

pect formation and accretion alone to generate a distribution with a smooth high-mass tail. The Gaussian mixture models used here are flexible enough to capture a smooth tail, even if it were skewed to give non-Gaussian (eg., steeper) dropoff; since the data preferred a sharp cut-off under our flexible model, we attribute the maximum mass cut-off to the EoS. Nevertheless, understanding the detailed formation and accretion physics and selection effects that underpin the inferred mass distribution is crucial to building confidence (or otherwise) in this conclusion.

*What would happen if we observed a  $2.1M_{\odot}$  neutron star?*

It is interesting to ask what would happen to our constraints on  $m_{\max}$  if we measured (with good precision) a neutron star with around  $2.1M_{\odot}$ , i.e. around the peak of the  $m_{\max}$  posterior (Fig. 3). We find that adding a sharply measured  $2.1M_{\odot}$  NS into the mass dataset shifts the lower limit on  $m_{\max}$  up to around  $2.1M_{\odot}$  (as one would expect), but otherwise the shape of the  $m_{\max}$  posterior, including the tail out to high masses, is largely unchanged. This makes good sense: in order to better constrain the location of the cut-off in the mass distribution from above, the high-mass end of the mass distribution needs to be better resolved. This can only be achieved with more measured masses around the high-mass end of the distribution.

## 6 CONSTRAINTS ON THE NEUTRON STAR EOS FROM THE INFERRED $m_{\max}$

Every EoS has associated with it a maximum stable NS mass that can be determined by solving the Tolman-Oppenheimer-Volkoff (TOV) structure equations (Tolman 1939; Oppenheimer & Volkoff 1939). As such, observational bounds on the maximum NS mass provide corresponding constraints on the NS EoS. Recent observations of  $2M_{\odot}$  NSs (Antoniadis et al. 2013; Demorest et al. 2010; Fonseca et al. 2016) have already ruled out some EoS models, and the requirement to support  $> 2M_{\odot}$  NSs has become one of the key requirements for the nuclear EoS at ultra-high densities.

From our inference of  $m_{\max}$ , the posterior probability of a model EoS with a given  $m_{\max}^{\text{EoS}}$  is given by

$$P(\text{EoS}|\mathbf{d}) = P(m_{\max} = m_{\max}^{\text{EoS}}|\mathbf{d}), \quad (12)$$

where the right hand side is just the posterior density shown in Fig. 3.

Throughout this section we will compute maximum masses by solving the TOV equations for slowly rotating NSs. This is justified, since NSs in binaries are neither expected nor observed to have spin periods much less than  $\lesssim 1.5\text{ms}$  (Chakrabarty 2008; Papitto et al. 2014; Miller & Miller 2015; Patruno et al. 2017). At these rotation rates, corrections to the mass due to rotation are less than a few percent, and typically much less<sup>7</sup> (Cook et al. 1994; Ster-

<sup>7</sup> Even at the extreme, mass-shedding limit, the mass of a nonrotating maximum mass neutron stars increases at most by  $\sim 20\%$  due to rotation (Breu & Rezzolla 2016), this value being smaller for lower mass stars (Cook et al. 1994). For reference, the fastest spinning pulsar in a binary, PSR J1748-2446ad (Hessels et al. 2006) has a spin period of  $\sim 1.4\text{ms}$ , a factor of  $\sim 1.5$  larger than the

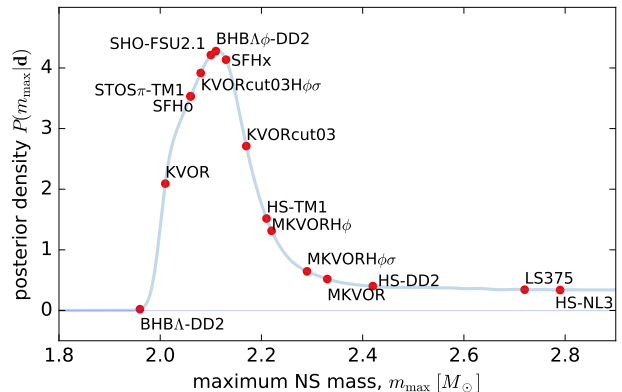


**Figure 5.** Constraints on tabulated equations-of-state from the inferred posterior distribution of  $m_{\max}$  derived from the NS mass distribution.

gioulas & Friedman 1995; Berti & Stergioulas 2004; Berti et al. 2005; Yagi et al. 2014).

In the following we explore constraints on the most up-to-date tabulated EoS models. In §6.2 we constrain a parameterized piecewise-polytropic model for the EoS and obtain bounds on the maximum sound speed attained inside NSs.

### 6.1 Constraints on numerical EoS models

In Table 4 we list a selection of nuclear physics-based tabulated EoS models, along with their respective maximum NS masses. This set of EoS tables is not intended to be exhaustive: for a more complete catalog, see e.g. Oertel et al. (2017). Fig. 5 shows the relative posterior probabilities of these EoSs given our posterior inference of  $m_{\max}$  (also tabulated in Table 4), computed from Eq. (12). From Fig. 5 it is clear that our analysis of the NS mass distribution strongly favors some EoS models relative to others, at odds ratios of up to 12 : 1 (see also Table 4). This is a vast improvement over previous maximum mass considerations, where any EoS that supported NSs with  $\gtrsim 2M_{\odot}$  was considered equally acceptable based on maximum mass considerations alone.

Whilst caution is justified since our results are derived from a still relatively small sample of 74 measured NS masses, the robustness of our results to model choice and data cuts demonstrated in §5.1 builds confidence in these constraints. Furthermore, our results fall nicely in line with independent constraints on the maximum NS mass derived from the assumption that short GRBs are produced primarily by coalescing NSs with rapidly collapsing remnants (Lawrence et al. 2015; Fryer et al. 2015). This begins to paint a coherent picture of upper limits on the maximum NS mass from astrophysical observations and considerations, and tightens our grip on  $m_{\max}$ .

mass-shedding frequency for a rotating NS (Lattimer & Prakash 2004) if we consider a fiducial nonrotating massive NS with mass  $M = 2M_{\odot}$  and radius  $R = 14\text{km}$ .

EoS	Exotic d.o.f	$m_{\max}$	posterior probability	reference(s)
HS-DD2		2.42	0.402	Hempel & Schaffner-Bielich (2010); Fischer et al. (2014)
SFHo		2.06	3.532	Steiner et al. (2013b)
SFHx		2.13	4.136	Steiner et al. (2013b)
HS-NL3		2.79	0.337	Hempel & Schaffner-Bielich (2010); Fischer et al. (2014)
SHO-FSU2.1		2.12	4.262	Shen et al. (2011)
LS375		2.72	0.343	Lattimer & Swesty (1991)
HS-TM1		2.21	1.512	Hempel & Schaffner-Bielich (2010); Hempel et al. (2012)
KVOR		2.01	2.092	Kolomeitsev & Voskresensky (2005); Klähn et al. (2006)
MKVOR		2.33	0.519	Maslov et al. (2016)
KVORcut03		2.17	2.711	Maslov et al. (2016)
KVORcut03H $\phi\sigma$	H, $\phi$ , H $\sigma$ scaling	2.08	3.917	Maslov et al. (2016)
MKVORH $\phi$	H, $\phi$	2.22	1.313	Maslov et al. (2016)
MKVORH $\phi\sigma$	H, $\phi$ , H $\sigma$ scaling	2.29	0.646	Maslov et al. (2016)
BBHA-DD2	H	1.96	0.020	Banik et al. (2014)
BBHA $\phi$ -DD2	H, $\phi$	2.11	4.278	Banik et al. (2014)
STOS $\pi$ -TM1	$\pi$	2.06	3.532	Nakazato et al. (2008)

**Table 4.** Maximum NS mass predictions and their associated posterior probabilities  $P(m_{\max}|\mathbf{d})$  (c.f. Fig. 5) for a selection of tabulated NS equations-of-state. Additional exotic species are denoted by H (Hyperons),  $\pi$  (pions),  $\phi$  ( $\phi$ -mesons) and  $\sigma$  ( $\sigma$ -mesons).

## 6.2 Constraints on piecewise polytropic EoS

### 6.2.1 Piecewise polytropic model

Representing the EoS as a piecewise polytrope has been demonstrated to be a useful parameterized model for the EoS<sup>8</sup> (Read et al. 2009; Özel & Psaltis 2009; Hebeler et al. 2013; Steiner et al. 2016; Raithel et al. 2016). Recently Raithel et al. (2016) showed that five polytropic nodes are required above the nuclear saturation density  $\rho_{\text{sat}} = 2.7 \times 10^{14} \text{g cm}^{-3}$  in order to reproduce the mass, radius, and moment of inertia for a range of realistic EoSs within the expected uncertainties of next-generation experiments (within 0.5km,  $0.1M_{\odot}$ , and 10% respectively). In this work we follow Raithel et al. (2016) and construct a five-node piecewise-polytropic EoS above the saturation density, described by:

$$P(\rho) = K_i \rho^{\Gamma_i}, \quad \rho_{i-1} < \rho < \rho_i, \quad (13)$$

where the polytropic indices  $\Gamma_i$  and normalization constants  $K_i$  are determined by the pressures and densities at the knots,

$$\Gamma_i = \frac{\ln(P_i/P_{i-1})}{\ln(\rho_i/\rho_{i-1})}, \quad K_i = \frac{P_i}{\rho_i^{\Gamma_i}}. \quad (14)$$

Following Raithel et al. (2016), we define five density knots at  $[1.4, 2.2, 3.3, 4.9, 7.4]\rho_{\text{sat}}$ , i.e. keeping the pressures at those densities  $\mathbf{p} = (P_1, P_2, P_3, P_4, P_5)$  as our free model parameters of interest.

Below  $0.6\rho_{\text{sat}}$  we assume a fixed SLy EoS for the crust taken from Douchin & Haensel (2001). Between  $0.6\rho_{\text{sat}}$  and  $1.1\rho_{\text{sat}}$ , the EoS is well constrained by chiral effective field theory calculations (Tews et al. 2013; Hebeler et al. 2013; Krüger et al. 2013). We assume the EoS in this regime is constrained to lie between the soft and stiff limits tabulated in Hebeler et al. (2013); to implement this constraint, we introduce two additional polytropic knots at  $\rho_1^* = 0.6\rho_{\text{sat}}$  and  $\rho_2^* = 1.1\rho_{\text{sat}}$ , where the pressures at those

densities are tightly constrained to fall in the ranges  $P_1^* \in [0.447, 0.696] \text{ MeV fm}^{-3}$  and  $P_2^* \in [2.163, 3.542] \text{ MeV fm}^{-3}$  respectively (taken from Table 5 of Hebeler et al. (2013)).

### 6.2.2 Physical constraints and priors

In addition to assumptions about the EoS below  $1.1\rho_{\text{sat}}$ , we impose some additional physical constraints and priors at higher densities. We require that the EoS be microscopically stable, i.e.  $P(\rho)$  must be strictly increasing:

$$P_i > P_{i-1}. \quad (15)$$

We also require that the EoS does not violate causality, i.e. the local sound speed is smaller than the speed of light:

$$\frac{dP}{d\epsilon} = \frac{c_s^2}{c^2} \leq 1. \quad (16)$$

Finally, some important constraints on the EoS at densities near  $\rho_{\text{sat}}$  come from nuclear scattering experiments at energies below 350MeV (Özel et al. 2016; Raithel et al. 2017); we impose lower limits on the pressures at the first two knots  $P_1 \geq 3.60 \text{ MeV fm}^{-3}$  and  $P_2 \geq 11.70 \text{ MeV fm}^{-3}$  to be consistent with nucleon-nucleon scattering data (following Özel et al. 2016; see also Akmal et al. 1998; Pieper et al. 2001; Gandolfi et al. 2014; Raithel et al. 2017).

### 6.2.3 Bayesian inference of polytropic EoS in light of the measurement of $m_{\max}$

As for the numerical EoS considered in 6.1, each piecewise-polytropic EoS  $P(\rho; \mathbf{p})$  has associated with it a maximum stable NS mass  $m_{\max} = m_{\max}(\mathbf{p})$ , that can be found by integrating the TOV equations as before. We can hence use the likelihood for the maximum NS mass obtained in §5.1 to perform posterior inference for the polytropic EoS parameters  $\mathbf{p}$ :

$$P(\mathbf{p}|\mathbf{d}) \propto P(\mathbf{d}|\mathbf{p})P(\mathbf{p}) = P(\mathbf{d}|m_{\max}(\mathbf{p}))P(\mathbf{p}), \quad (17)$$

where we will assume broad log-uniform priors  $P(\mathbf{p})$  additionally satisfying the constraints described in 6.2.2, and the

<sup>8</sup> Other useful parameterizations also exist: for example Lindblom (2010) performs a spectral decomposition of the EoS.

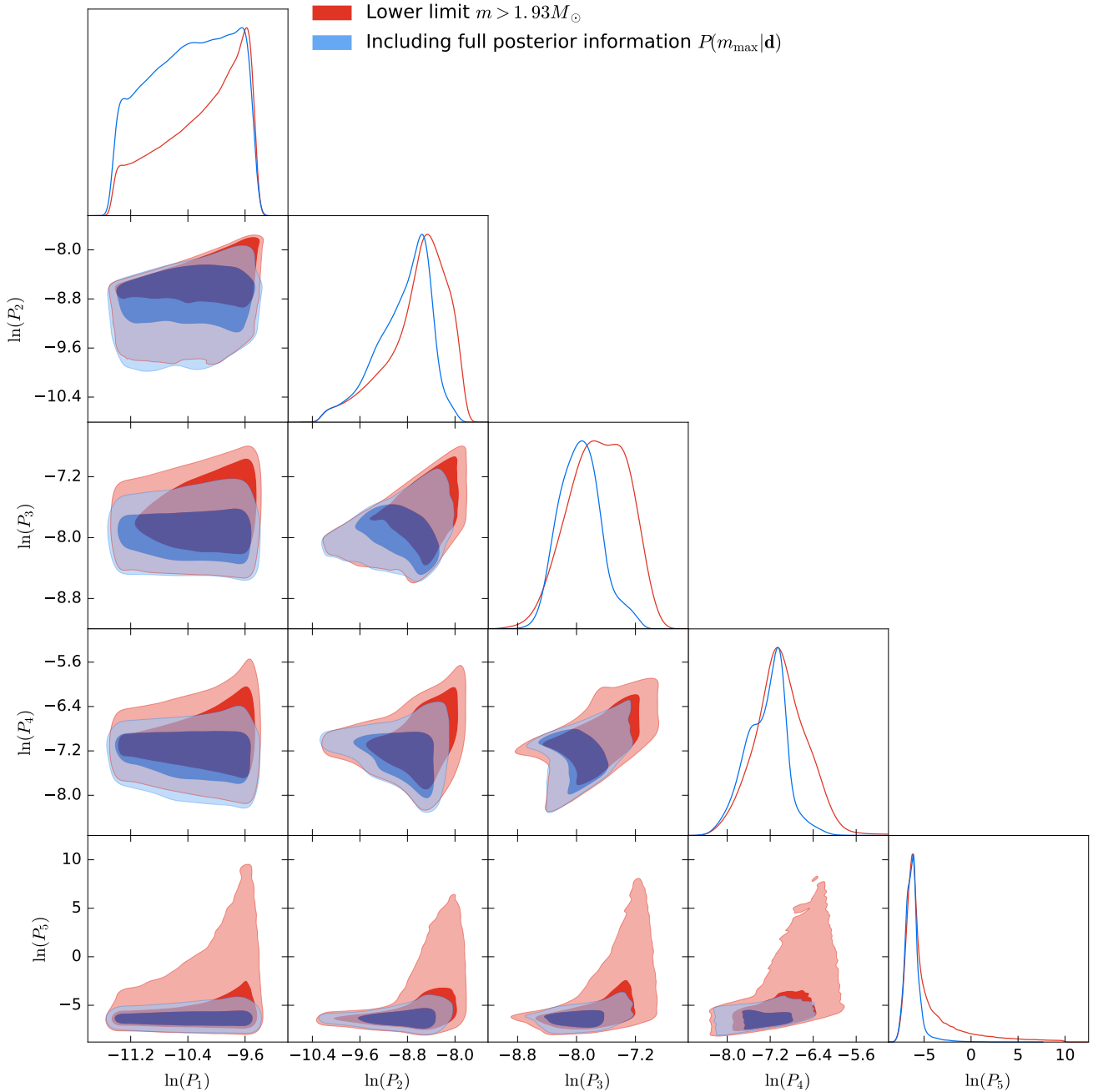


**Figure 6.** Comparison of posterior constraints on the NS equation-of-state parameterized by a 5-piece polytrope from assuming a lower limit on the maximum NS mass  $m_{\max} > 1.93M_{\odot}$  (red) compared to including full posterior information on the maximum mass derived from the mass distribution of NSs  $P(m_{\max}|d)$ .

likelihood  $P(\mathbf{d}|m_{\max}(\mathbf{p}))$  is given by Eq. (9) marginalized over the other mass-distribution parameters (cf. Fig. 3).

To quantify the extra information gained from our results over previous NS mass considerations, we consider two cases: one using the full  $P(\mathbf{d}|m_{\max})$  obtained in §5.1, and one just imposing  $P(\mathbf{d}|m_{\max}) \propto \Theta(m_{\max} - 1.93M_{\odot})$ , i.e. assuming all of the information about the maximum mass comes from the most massive precisely measured system J0348+0432 ( $m_p = 2.01(4)M_{\odot}$ ; Antoniadis et al. (2013)) requiring  $m_{\max} > 1.93M_{\odot}$  (95%). We sample the posterior for the polytropic parameters using affine-invariant ensemble

MCMC EMCEE (Foreman-Mackey et al. 2013); the posteriors are summarized in Fig. 6.

From Fig. 6 it's clear that including the full inference of the maximum mass from the NS mass distribution constrains the allowed parameter space of the piecewise polytrope EoS compared to simply taking a lower bound for  $m_{\max}$ , with the improvement being most significant for  $P_3$ ,  $P_4$  and  $P_5$  at  $\rho_3 = 3.3\rho_{\text{sat}}$ ,  $\rho_4 = 4.9\rho_{\text{sat}}$  and  $\rho_5 = 7.4\rho_{\text{sat}}$  respectively. The 68% credible regions of the marginalized posteriors for  $P_3$ ,  $P_4$  and  $P_5$  are improved by 35, 30 and 50% respectively. Note that the tail out to high values of  $P_5$  (par-

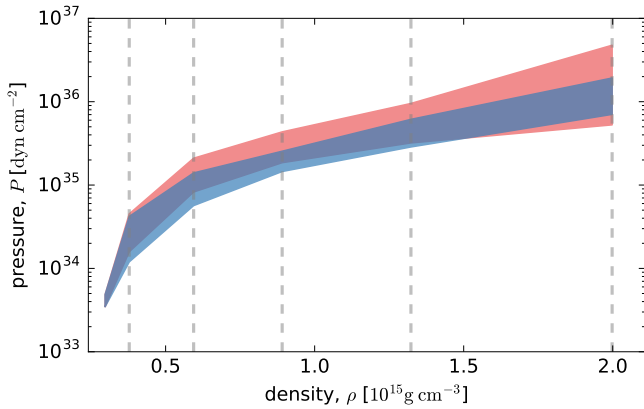


**Figure 7.** Constraints on the piecewise polytropic EoS from the full posterior distribution for  $m_{\max}$  derived from the NS mass distribution (blue), and just assuming a lower limit on the maximum NS mass  $m_{\max} > 1.93M_{\odot}$  (red). The bands indicate the 68% credible regions for the pressure at the nodes  $[1.4, 2.2, 3.3, 4.9, 7.4]\rho_{\text{sat}}$  indicated by the vertical grey lines. Note that the credible regions shown correspond to the 1d marginals; Fig. 6 shows the correlation structure of the inferred polytropic EoS parameters. Assumptions about the EoS at densities  $< 1.1\rho_{\text{sat}}$  (far left) are described in §6.2.

ticularly for the  $m_{\max} > 1.93M_{\odot}$  contours) are a result of the fact that when  $P_1, \dots, P_4$  are sufficiently large, the maximum central density may be close to or smaller than  $\rho_4$ , in which cases  $P_5$  is unconstrained. This is a weakness of the piecewise polytrope set-up for the EoS and may be alleviated by an alternative EoS parameterization.

Fig. 7 shows the constraints on the piecewise polytropic EoS  $P(\rho)$ ; the bands show the 68% credible regions of the 1d marginal posteriors of the polytropic parameters using full posterior information on  $m_{\max}$  (blue) versus just assuming a lower limit  $m_{\max} > 1.93M_{\odot}$  (red). Whilst the correlations between the polytropic parameters are not captured by this figure, the 30–50% improvement on the inferred EoS at  $3\text{--}7 \times \rho_{\text{sat}}$  is clearly shown.

There is an open debate on whether the causal limit  $c_s < c$  is strict enough, with some authors making theoretical arguments why  $c_s < c/\sqrt{3}$  may be a more appropriate bound (Weinberg 1972; Lattimer 2014; Bedaque & Steiner 2015; Moustakidis et al. 2017). In Fig. 8 we show the posterior constraints on the maximum speed of sound attained inside the NS under our piecewise polytropic model for the EoS. We find a lower bound on the maximum sound speed of  $c_s^{\max} > 0.63c$  (99.8%), ruling out  $c_s < c/\sqrt{3}$  at very high significance. This tension was also discussed in Bedaque & Steiner (2015). Kurkela et al. (2014) found that  $c_s^{\max} > 0.74$  based on maximum mass considerations, although cautioned that their constraint may be overly restrictive.

### 6.3 Comparison to other astrophysical constraints on the EoS

In addition to maximum mass considerations, there are a number of other constraints on the NS EoS from astrophysical observations.

Measurements of NS masses and radii together can put

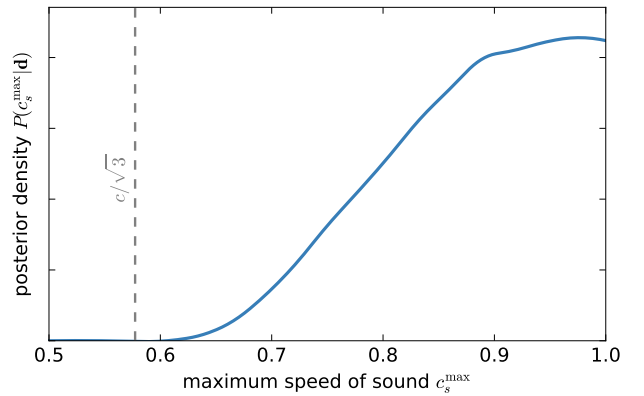


**Figure 8.** Marginal posterior distribution for the maximum sound speed attained inside the NS, derived from  $P(m_{\max}|\mathbf{d})$  using the 5-piece polytropic model for the EoS. The lower limit is  $c_s^{\max} > 0.63c$  (99.8%), ruling out  $c_s < c/\sqrt{3}$  at high significance as shown by the vertical dashed line.

strong constraints on the EoS (Read et al. 2009; Özel & Psaltis 2009; Özel et al. 2010; Steiner et al. 2010; Guillot et al. 2013; Steiner et al. 2013a,b; Özel et al. 2016). Measuring radii from x-ray observations is much more complicated than mass determination, and inferences are typically more model dependent; atmospheric composition, magnetic fields, source distance, interstellar extinction, residual accretion, brightness variations over the surface, and the effects of rotation in sources with unknown spin frequencies can all introduce systematic errors and must be carefully accounted for (Miller 2013; Potekhin 2014; Fortin et al. 2015; Özel et al. 2016). Whilst there is not yet firm consensus amongst NS radii measurements, advances have been made in accounting for systematic errors and strong (although model dependent) constraints on the EoS have been obtained (see eg., Özel et al. (2016) for an attempt to account for a multitude of systematics). Radius measurements are most sensitive to the EoS around  $\sim 2 \times \rho_{\text{sat}}$ , so they are complementary to the maximum mass constraints, which probe higher densities  $\gtrsim 3 \times \rho_{\text{sat}}$ .

In Fig. 9 we compare the marginal constraints on the polytropic EoS from our work (blue) to the mass-radius measurement analysis of Özel et al. (2016) (red). Note that we use a more flexible five-node polytropic EoS, whereas Özel et al. (2016) use a three-node EoS with nodes at  $[1.85, 3.7, 7.4]\rho_{\text{sat}}$ , but very similar prior assumptions otherwise (see Özel et al. 2016 for details). As expected, the mass-radius measurements are more constraining than maximum-mass considerations alone, giving  $\sim 4\times$  stronger constraints at  $\sim 2\rho_{\text{sat}}$  where the mass-radius data are most informative, and  $\sim 2\times$  stronger constraints above  $2\rho_{\text{sat}}$ . Although caution is deserved directly comparing the three- and five-node polytropic models, the figure gives some idea of the relative constraining power of these data under similar prior assumptions, and indicates statistical consistency between the two analyses.

In Fig. 10 we compare our constraints on the EoS to the

mass-radius measurement analysis of Steiner et al. (2013a)<sup>9</sup>. In order to compare with Steiner et al. (2013a), we converted our constraints from  $P(\rho)$  to  $P(\epsilon)$  (pressure as a function of energy density), using the relation  $d(\epsilon/\rho) = -P d(1/\rho)$ . Since Steiner et al. (2013a) consider a more flexible suite of models for the EoS compared to our piecewise polytrope, this figure does not indicate the relative constraining power of the two datasets, but does demonstrate that our constraints are in good agreement with Steiner et al. (2013a).

Gravitational wave observations of coalescing NS-NS or NS-black hole binaries with Advanced LIGO and VIRGO are expected to put constraints on the EoS primarily via determination of the NS tidal deformability (Del Pozzo et al. 2013; Agathos et al. 2015; Lackey & Wade 2015). The recent observation of the NS-NS merger GW170817 (Abbott et al. 2017) marks the dawn of a new era in probing NS physics with gravitational waves, and it is already providing new insights on the EoS (Annala et al. 2017; Banik & Bandyopadhyay 2017; Radice et al. 2018; Most et al. 2018; Zhang et al. 2018). We leave a direct comparison with these observations (and improved, combined constraints) to future work.

A measurement of the moment of inertia of NSs may be possible through observations of spin-orbit coupling effects in binaries, namely precession of the orbital plane and higher-order contributions to the periastron advance (Lyne et al. 2004; Lattimer & Schutz 2005). Such a measurement would provide further constraints on the EoS, particularly at  $\sim 2 \times \rho_{\text{sat}}$  (Lattimer & Schutz 2005), but sufficiently precise observations are expected to be some years away (Lattimer & Prakash 2016).

It has also been suggested that the lightest NSs may be used to constrain the EoS via their formation history (Podsiadlowski et al. 2005), although this approach typically leads to highly model dependent constraints.

## 7 CONCLUSIONS

We have inferred the NS mass distribution from all currently available pulsar mass measurements using a flexible  $n$ -component Gaussian mixture model, allowing for a maximum mass cut-off. We find strong evidence for a bimodal distribution (Bayes factor  $2\ln\mathcal{K} > 10$ ), in agreement with previous literature. Increasing the number of Gaussian components in the mixture model does not elicit further distinct peaks, and the model with  $n = 2$  components is the most preferred.

We report, for the first time, positive evidence for a sharp cut-off in the NS mass distribution; for all Gaussian mixture models considered with  $n \geq 2$  components, the truncated models with  $m_{\text{max}}$  as a free parameter are preferred over those with fixed  $m_{\text{max}} = 2.9M_{\odot}$  with Bayes factors  $2\ln\mathcal{K} \gtrsim 3$  (Table 2). We inferred the marginal posterior distribution for the maximum NS mass (Fig. 3) and obtained  $2.0M_{\odot} < m_{\text{max}} < 2.2M_{\odot}$  (68%) and  $2.0M_{\odot} < m_{\text{max}} < 2.6M_{\odot}$  (90%) credible regions for  $m_{\text{max}}$ . These constraints on  $m_{\text{max}}$  are robust to the number of Gaussian components

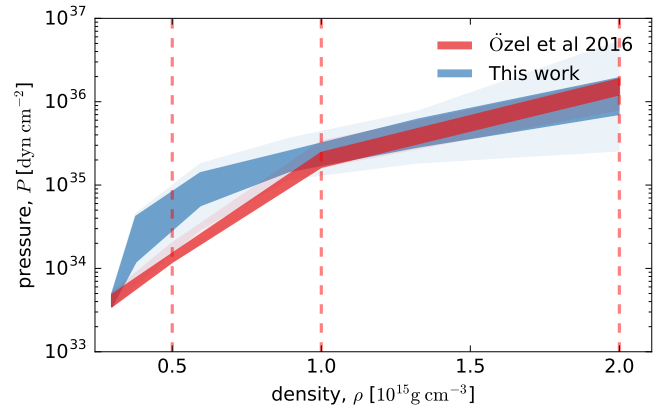


**Figure 9.** Comparison of constraints on the piecewise polytropic EoS from the derived posterior distribution for  $m_{\text{max}}$  (this work; blue), and neutron star mass-radius measurements from Özel et al. 2016 (red). The bands indicate the 68 and 95% credible regions. The nodes of the five-node polytrope (this work) are at densities  $[1.4, 2.2, 3.3, 4.9, 7.4]\rho_{\text{sat}}$ , whilst Özel et al. (2016) used a three-node polytrope with nodes at  $[1.85, 3.7, 7.4]\rho_{\text{sat}}$ , indicated by the red-dashed lines. Credible regions shown correspond to the 1d marginals; the correlation structure of the inferred EoS parameters is not captured by this plot (cf. Fig. 6). Priors and assumptions about the EoS at densities  $< 1.1\rho_{\text{sat}}$  (far left) are similar in the two studies (see §6.2).

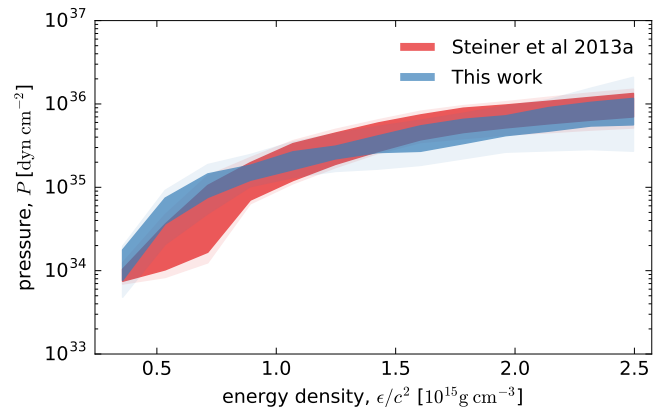


**Figure 10.** Comparison of constraints on the EoS from the derived posterior distribution for  $m_{\text{max}}$  (this work; blue), and neutron star mass-radius measurements (Steiner et al. 2013a; red). The bands indicate the 68 and 95% credible regions. Although Steiner et al. (2013a) consider a more flexible suite of EoS parameterizations compared to our five-node polytrope, the constraints are in good agreement. Note that our constraints on  $P(\rho)$  (Figs. 6, 7 and 9) were converted to  $P(\epsilon)$  for direct comparison with Steiner et al. (2013a).

included in the mixture model for  $n = 2, \dots, 4$ , where increasing the number of components tightens the constraints and increases the Bayes factor modestly (Fig. 4).

The evidence for and constraint on the  $m_{\text{max}}$  cut-off are robust against removing key subsets of the data, demonstrating that the observed maximum mass cut-off is driven by the shape of the NS mass distribution, informed by the

<sup>9</sup> The EoS constraints from Steiner et al. (2013a) are publicly available at <https://web.utk.edu/~asteine1/slb13.html>

whole population, rather than set by the most extreme (massive) objects (Fig. 4). The lower bound on  $m_{\max}$  is mostly set by the most massive precisely measured masses, namely J0348+0432 and J1614-2230 (both close to  $2M_{\odot}$ ), but the reported positive evidence for the maximum mass cut-off persists with these systems removed. Similarly, J1748-2021B is likely to be even more massive (although more uncertain), but leaving it out of the dataset had a negligible impact on our conclusions. X-ray/optical mass measurements potentially suffer from residual systematics that could be biasing the  $m_{\max}$  inference; we found that with these systems removed from the data, positive evidence for the sharp cut-off persists, and the inferred  $m_{\max}$  was modestly impacted.

Our constraints on the maximum NS mass are in good agreement with, and independent of, recent studies of short GRBs, where Lawrence et al. (2015) and Fryer et al. (2015) argue that  $m_{\max} \lesssim 2.2 - 2.5M_{\odot}$  is required assuming that the main source of short GRBs are NS-NS mergers. On the flip side, our constraints on the maximum NS mass show a strong preference for equations of state for which short GRBs are produced in NS-NS mergers, strengthening the case for NS mergers as the primary source of short GRBs. Our constraints on  $m_{\max}$  are also in excellent agreement with the observations of the binary neutron star merger GW170817 (Abbott et al. 2017), which have been used to constrain  $m_{\max} < 2.17M_{\odot}$  (90%) (Margalit & Metzger 2017),  $m_{\max} < 2.33M_{\odot}$  (90%) (Rezzolla et al. 2018),  $m_{\max} < 2.16 - 2.28M_{\odot}$  (Ruiz et al. 2018).

Using our inference of the maximum NS mass we are able to put tight constraints on the NS equation of state. We find that for a set of realistic EoSs that support  $> 2M_{\odot}$  NSs, our inference of  $m_{\max}$  is able to distinguish between models at odds ratios of up to 12:1 based on maximum mass considerations alone (Fig. 5). Considering a parameterized five-node polytropic equation of state, we are able to obtain constraints on the pressure at densities of  $3-7 \times \rho_{\text{sat}}$  that are improved by 30–50% compared to simply assuming  $m_{\max} > 1.93M_{\odot}$  (Figs. 6–7). Under this piecewise polytropic EoS model, we find a lower bound on the maximum sound speed attained inside the NS of  $c_s^{\max} > 0.63c$  (99.8%), ruling out  $c_s < c/\sqrt{3}$  at high significance (Fig. 8). Our constraints on the EoS from maximum mass considerations are in good agreement with neutron star mass-radius measurements (Steiner et al. 2013a; Özel et al. 2016).

## ACKNOWLEDGMENTS

We thank Feryal Özel, Kenta Hotokezaka, Stephen Feeney, Paulo Freire and John Antoniadis for useful discussions, and Feryal Özel for kindly providing the data used for comparison in Fig. 9. E. B. was supported by NSF Grants No. PHY-1607130 and AST-1716715, and by FCT contract IF/00797/2014/CP1214/CT0012 under the IF2014 Programme. H. O. S was supported by NSF Grant No. PHY-1607130 and NASA grant NNX16AB98G and 80NSSC17M0041. H. O. S also thanks Thomas Sotiriou and the University of Nottingham for hospitality.

## REFERENCES

Abadie J., et al., 2010, *Classical and Quantum Gravity*, 27, 173001

- Abbott B. P., et al., 2017, *Physical Review Letters*, 119, 161101
- Agathos M., Meidam J., Del Pozzo W., Li T. G., Tompitak M., Veitch J., Vitale S., Van Den Broeck C., 2015, *Physical Review D*, 92, 023012
- Akmal A., Pandharipande V., Ravenhall D., 1998, *Physical Review C*, 58, 1804
- Althaus L. G., Bertolami M. M. M., Córscico A. H., 2013, *Astronomy & Astrophysics*, 557, A19
- Annala E., Gorda T., Kurkela A., Vuorinen A., 2017, arXiv preprint arXiv:1711.02644
- Antoniadis J., van Kerkwijk M. H., Koester D., Freire P. C. C., Wex N., Tauris T. M., Kramer M., Bassa C. G., 2012, *Mon. Not. Roy. Astron. Soc.*, 423, 3316
- Antoniadis J., et al., 2013, *Science*, 340, 1233232
- Antoniadis J., Tauris T. M., Ozel F., Barr E., Champion D. J., Freire P. C., 2016, arXiv preprint arXiv:1605.01665
- Arzoumanian Z., et al., 2017, arXiv preprint arXiv:1801.01837
- Banik S., Bandyopadhyay D., 2017, arXiv preprint arXiv:1712.09760
- Banik S., Hempel M., Bandyopadhyay D., 2014, *The Astrophysical Journal Supplement Series*, 214, 22
- Barr E., Freire P., Kramer M., Champion D., Berezhina M., Bassa C., Lyne A., Stappers B., 2016, *Monthly Notices of the Royal Astronomical Society*, 465, 1711
- Bassa C. G., van Kerkwijk M. H., Koester D., Verbunt F., 2006, *Astron. Astrophys.*, 456, 295
- Bedaque P., Steiner A. W., 2015, *Physical review letters*, 114, 031103
- Berezhina M., et al., 2017, *MNRAS*, 470, 4421
- Berti E., Stergioulas N., 2004, *Mon. Not. Roy. Astron. Soc.*, 350, 1416
- Berti E., White F., Maniopoulou A., Bruni M., 2005, *Mon. Not. Roy. Astron. Soc.*, 358, 923
- Bhalerao V., van Kerkwijk M. H., Harrison F., 2012, *The Astrophysical Journal*, 757, 10
- Bhat N. D. R., Bailes M., Verbiest J. P. W., 2008, *Phys. Rev.*, D77, 124017
- Breu C., Rezzolla L., 2016, *Monthly Notices of the Royal Astronomical Society*, 459, 646
- Buchner J., et al., 2014, *Astronomy & Astrophysics*, 564, A125
- Casares J., Hernandez J. I. G., Israelian G., Reboloto R., 2010, *Mon. Not. Roy. Astron. Soc.*, 401, 2517
- Chakrabarty D., 2008, in Wijnands R., Altamirano D., Soleri P., Degenaar N., Rea N., Casella P., Patruno A., Linares M., eds, *American Institute of Physics Conference Series Vol. 1068*, American Institute of Physics Conference Series. pp 67–74 (arXiv:0809.4031), doi:10.1063/1.3031208
- Chruslinska M., Belczynski K., Klencki J., Benacquista M., 2017, arXiv preprint arXiv:1708.07885
- Cognard I., et al., 2017, *ApJ*, 844, 128
- Cook G. B., Shapiro S. L., Teukolsky S. A., 1994, *The Astrophysical Journal*, 424, 823
- Del Pozzo W., Li T. G., Agathos M., Van Den Broeck C., Vitale S., 2013, *Physical review letters*, 111, 071101
- Deller A. T., et al., 2012, *The Astrophysical Journal*, 756, L25
- Demorest P., Pennucci T., Ransom S., Roberts M., Hessels J., 2010, *Nature*, 467, 1081
- Deneva J. S., et al., 2012, *The Astrophysical Journal*, 757, 89
- Desvignes G., et al., 2016, *Monthly Notices of the Royal Astronomical Society*, 458, 3341
- Dominik M., et al., 2015, *The Astrophysical Journal*, 806, 263
- Douchin F., Haensel P., 2001, *Astronomy & Astrophysics*, 380, 151
- Falanga M., Bozzo E., Lutovinov A., Bonnet-Bidaud J., Fetisova Y., Puls J., 2015, *Astronomy & Astrophysics*, 577, A130
- Ferdman R. D., et al., 2010, *The Astrophysical Journal*, 711, 764
- Ferdman R. D., et al., 2014, *Mon. Not. Roy. Astron. Soc.*, 443, 2183

- Feroz F., Hobson M., 2008, *Monthly Notices of the Royal Astronomical Society*, 384, 449
- Feroz F., Hobson M., Bridges M., 2009, *Monthly Notices of the Royal Astronomical Society*, 398, 1601
- Ferraro F., Sabbi E., Gratton R., Possenti A., D'Amico N., Bragaglia A., Camilo F., 2003, *The Astrophysical Journal Letters*, 584, L13
- Finn L. S., 1994, *Physical review letters*, 73, 1878
- Fischer T., Hempel M., Sagert I., Suwa Y., Schaffner-Bielich J., 2014, *The European physical journal A*, 50, 46
- Fonseca E., Stairs I. H., Thorsett S. E., 2014, *The Astrophysical Journal*, 787, 82
- Fonseca E., et al., 2016, *The Astrophysical Journal*, 832, 167
- Foreman-Mackey D., Hogg D. W., Lang D., Goodman J., 2013, *Publications of the Astronomical Society of the Pacific*, 125, 306
- Fortin M., Zduunik J., Haensel P., Bejger M., 2015, *Astronomy & Astrophysics*, 576, A68
- Freire P. C., Ransom S. M., Gupta Y., 2007, *The Astrophysical Journal*, 662, 1177
- Freire P. C., Ransom S. M., Bégin S., Stairs I. H., Hessels J. W., Frey L. H., Camilo F., 2008a, *The Astrophysical Journal*, 675, 670
- Freire P. C. C., Wolszczan A., van den Berg M., Hessels J. W. T., 2008b, *ApJ*, 679, 1433
- Freire P. C. C., et al., 2017, *MNRAS*, 471, 857
- Fryer C. L., Kalogera V., 2001, *The Astrophysical Journal*, 554, 548
- Fryer C. L., Belczynski K., Ramirez-Ruiz E., Rosswog S., Shen G., Steiner A. W., 2015, *The Astrophysical Journal*, 812, 24
- Gandolfi S., Carlson J., Reddy S., Steiner A., Wiringa R., 2014, *The European Physical Journal A*, 50, 10
- Gelino D. M., Tomsick J. A., Heindl W. A., 2002, in *American Astronomical Society Meeting Abstracts*. p. 1199
- Guillot S., Servillat M., Webb N. A., Rutledge R. E., 2013, *The Astrophysical Journal*, 772, 7
- Hebeler K., Lattimer J., Pethick C. J., Schwenk A., 2013, *The Astrophysical Journal*, 773, 11
- Hempel M., Schaffner-Bielich J., 2010, *Nuclear Physics A*, 837, 210
- Hempel M., Fischer T., Schaffner-Bielich J., Liebendörfer M., 2012, *The Astrophysical Journal*, 748, 70
- Hessels J. W. T., Ransom S. M., Stairs I. H., Freire P. C. C., Kaspi V. M., Camilo F., 2006, *Science*, 311, 1901
- Horvath J., Valentim R., 2016, arXiv preprint arXiv:1607.06981
- Istrate A., Tauris T., Langer N., Antoniadis J., 2014, *Astronomy & Astrophysics*, 571, L3
- Jacoby B. A., Cameron P. B., Jenet F. A., Anderson S. B., Murty R. N., Kulkarni S. R., 2006, *The Astrophysical Journal*, 644, L113
- Joss P., Rappaport S., 1976, *Nature*, 264, 219
- Kalogera V., Baym G., 1996, *The Astrophysical Journal Letters*, 470, L61
- Kaplan D. L., Bhalerao V. B., van Kerkwijk M. H., Koester D., Kulkarni S. R., Stovall K., 2013, *The Astrophysical Journal*, 765, 158
- Kass R. E., Raftery A. E., 1995, *Journal of the American Statistical Association*, 90, 773
- Kiziltan B., Kottas A., De Yoreo M., Thorsett S. E., 2013, *The Astrophysical Journal*, 778, 66
- Klähn T., et al., 2006, *Physical Review C*, 74, 035802
- Kolomeitsev E., Voskresensky D., 2005, *Nuclear Physics A*, 759, 373
- Kramer M., et al., 2006, *Science*, 314, 97
- Krüger T., Tews I., Hebeler K., Schwenk A., 2013, *Physical Review C*, 88, 025802
- Kurkela A., Fraga E. S., Schaffner-Bielich J., Vuorinen A., 2014, *The Astrophysical Journal*, 789, 127
- Lackey B. D., Wade L., 2015, *Physical Review D*, 91, 043002
- Lattimer J., 2014, *Astrophysics and Cosmology: Proceedings of the 26th Solvay Conference on Physics* (Editors: R. Blandford, D. Gross and A. Sevrin, 2014, World Scientific)
- Lattimer J. M., Prakash M., 2004, *Science*, 304, 536
- Lattimer J. M., Prakash M., 2016, *Physics Reports*, 621, 127
- Lattimer J. M., Schutz B. F., 2005, *The Astrophysical Journal*, 629, 979
- Lattimer J. M., Swesty F. D., 1991, *Nuclear Physics A*, 535, 331
- Lawrence S., Tervala J. G., Bedaque P. F., Miller M. C., 2015, *The Astrophysical Journal*, 808, 186
- Lazarus P., et al., 2016, *ApJ*, 831, 150
- Lindblom L., 2010, *Physical Review D*, 82, 103011
- Lynch R. S., Freire P. C. C., Ransom S. M., Jacoby B. A., 2012, *The Astrophysical Journal*, 745, 109
- Lyne A. G., et al., 2004, *Science*, 303, 1153
- Margalit B., Metzger B. D., 2017, *The Astrophysical Journal Letters*, 850, L19
- Martinez J. G., et al., 2015, *The Astrophysical Journal*, 812, 143
- Maslov K., Kolomeitsev E., Voskresensky D., 2016, *Nuclear Physics A*, 950, 64
- Miller M. C., 2013, arXiv preprint arXiv:1312.0029
- Miller M. C., Miller J. M., 2015, *Physics Reports*, 548, 1
- Most E. R., Weih L. R., Rezzolla L., Schaffner-Bielich J., 2018, arXiv preprint arXiv:1803.00549
- Moustakidis C. C., Gaitanos T., Margaritis C., Lalazissis G. A., 2017, *Phys. Rev.*, C95, 045801
- Munoz-Darias T., Casares J., Martinez-Pais I. G., 2005, *The Astrophysical Journal*, 635, 502
- Nakazato K., Sumiyoshi K., Yamada S., 2008, *Physical Review D*, 77, 103006
- Nice D. J., 2003, in *IAU Proceedings*.
- Oertel M., Hempel M., Klähn T., Typel S., 2017, *Reviews of Modern Physics*, 89, 015007
- Oppenheimer J. R., Volkoff G. M., 1939, *Physical Review*, 55, 374
- Özel F., Freire P., 2016, *Annual Review of Astronomy and Astrophysics*, 54, 401
- Özel F., Psaltis D., 2009, *Physical Review D*, 80, 103003
- Özel F., Baym G., Güver T., 2010, *Physical Review D*, 82, 101301
- Özel F., Psaltis D., Narayan R., Villarreal A. S., 2012, *The Astrophysical Journal*, 757, 55
- Özel F., Psaltis D., Güver T., Baym G., Heinke C., Guillot S., 2016, *The Astrophysical Journal*, 820, 28
- Papitto A., Torres D., Rea N., Tauris T., 2014, *Astronomy & Astrophysics*, 566, A64
- Patruno A., Haskell B., Andersson N., 2017, preprint (arXiv:1705.07669)
- Pieper S. C., Pandharipande V., Wiringa R. B., Carlson J., 2001, *Physical Review C*, 64, 014001
- Podsiadlowski P., Dewi J., Lesaffre P., Miller J. C., Newton W., Stone J. R., 2005, *Monthly Notices of the Royal Astronomical Society*, 361, 1243
- Potekhin A. Y., 2014, *Physics-Uspekhi*, 57, 735
- Radice D., Perego A., Zappa F., Bernuzzi S., 2018, *The Astrophysical Journal Letters*, 852, L29
- Raithel C. A., Özel F., Psaltis D., 2016, *The Astrophysical Journal*, 831, 44
- Raithel C. A., Özel F., Psaltis D., 2017, *The Astrophysical Journal*, 844, 156
- Ransom S. M., Hessels J. W., Stairs I. H., Freire P. C., Camilo F., Kaspi V. M., Kaplan D. L., 2005, *Science*, 307, 892
- Ransom S. M., et al., 2014, *Nature*, 505, 520
- Rawls M. L., Orosz J. A., McClintock J. E., Torres M. A. P., Bailyn C. D., Buxton M. M., 2011, *The Astrophysical Journal*, 730, 25
- Read J. S., Lackey B. D., Owen B. J., Friedman J. L., 2009, *Physical Review D*, 79, 124032

- Reardon D. J., et al., 2016, *Mon. Not. Roy. Astron. Soc.*, 455, 1751
- Rezzolla L., Most E. R., Weih L. R., 2018, *The Astrophysical Journal Letters*, 852, L25
- Rhoades Jr C. E., Ruffini R., 1974, *Physical Review Letters*, 32, 324
- Romani R. W., Filippenko A. V., Silverman J. M., Cenko S. B., Greiner J., Rau A., Elliott J., Pletsch H. J., 2012, *The Astrophysical Journal*, 760, L36
- Ruiz M., Shapiro S. L., Tsokaros A., 2018, *Physical Review D*, 97, 021501
- Schwab J., Podsiadlowski P., Rappaport S., 2010, *The Astrophysical Journal*, 719, 722
- Shen G., Horowitz C., O'Connor E., 2011, *Physical Review C*, 83, 065808
- Splaver E. M., Nice D. J., Arzoumanian Z., Camilo F., Lyne A. G., Stairs I. H., 2002, *The Astrophysical Journal*, 581, 509
- Stairs I. H., 2003, *Living Reviews in Relativity*, 6, 5
- Steehhs D., Jonker P. G., 2007, *The Astrophysical Journal*, 669, L85
- Steiner A. W., Lattimer J. M., Brown E. F., 2010, *The Astrophysical Journal*, 722, 33
- Steiner A. W., Lattimer J. M., Brown E. F., 2013a, *The Astrophysical Journal Letters*, 765, L5
- Steiner A. W., Hempel M., Fischer T., 2013b, *The Astrophysical Journal*, 774, 17
- Steiner A. W., Lattimer J. M., Brown E. F., 2016, *The European Physical Journal A*, 52, 18
- Stergioulas N., Friedman J. L., 1995, *ApJ*, 444, 306
- Stovall K., et al., 2016, In preparation
- Tews I., Krüger T., Hebel K., Schwenk A., 2013, *Physical review letters*, 110, 032504
- Thorsett S. E., Chakrabarty D., 1999, *The Astrophysical Journal*, 512, 288
- Tolman R. C., 1939, *Physical Review*, 55, 364
- Tremblay P.-E., Ludwig H.-G., Steffen M., Freytag B., 2013, *Astronomy & Astrophysics*, 552, A13
- Tremblay P.-E., Gianninas A., Kilic M., Ludwig H.-G., Steffen M., Freytag B., Hermes J., 2015, *The Astrophysical Journal*, 809, 148
- Valentim R., Rangel E., Horvath J., 2011, *Monthly Notices of the Royal Astronomical Society*, 414, 1427
- Van Kerkwijk M., Breton R., Kulkarni S., 2011, *The Astrophysical Journal*, 728, 95
- Weinberg S., 1972, *Gravitation and cosmology: principles and applications of the general theory of relativity*. Vol. 1, Wiley New York
- Weisberg J. M., Nice D. J., Taylor J. H., 2010, *The Astrophysical Journal*, 722, 1030
- Yagi K., Kyutoku K., Pappas G., Yunes N., Apostolatos T. A., 2014, *Phys. Rev.*, D89, 124013
- Zhang N.-B., Li B.-A., Xu J., 2018, arXiv preprint arXiv:1801.06855
- van Leeuwen J., et al., 2015, *The Astrophysical Journal*, 798, 118
- van Staden A. D., Antoniadis J., 2016, *The Astrophysical Journal Letters*, 833, L12